Journal of Power Sources 243 (2013) 750–757

Contents lists available at SciVerse ScienceDirect

Journal of Power Sources

journal homepage: www.elsevier.com/locate/jpowsour

Porosity and phase fraction evolution with aging in lithium iron phosphate battery cathodes

Samartha A. Channagiri [a], Shrikant C. Nagpure [b,*], S.S. Babu [a], Garret J. Noble [c], Richard T. Hart [c]

[a] Department of Materials Science and Engineering, Ohio State University, Columbus, OH 43210, USA
[b] Center for Automotive Research (CAR), Ohio State University, 930 Kinnear Rd., Columbus, OH 43212, USA
[c] Department of Bio-medical Engineering, Ohio State University, 1080 Carmack Rd., Columbus, OH 43210, USA

HIGHLIGHTS

- Multi-scale characterization of commercial $LiFePO_4$ cathodes as a function of location and aging.
- Characterization is non-destructive.
- X-Ray micro-CT has been used to measure porosity of the cathodes.
- XRD has been used to measure phase fraction evolution of the cathodes.
- Simultaneous porosity and phase fraction evolution compared and explained.

ARTICLE INFO

Article history:
Received 8 January 2013
Received in revised form
3 June 2013
Accepted 4 June 2013
Available online 13 June 2013

Keywords:
Li-ion Batteries
Aging
Tomography
Porosity
Phase fraction

ABSTRACT

Rechargeable Lithium-ion batteries designed for electric vehicles operate under different charge and discharge rates, state of charge and temperature . However, aging of these batteries due to disruption of ionic or electronic conductivity while operating under these different cycling conditions has been a concern. In this research, we measured statistical distribution of porosity in the cathode as a function of aging and location within the cylindrical battery, using X-Ray micro-computed tomography. A change in porosity (~20%) of the sample is noticed between aged and unaged samples. Concurrent X-Ray diffraction studies in these samples showed an increase (~34%) in $FePO_4$ phase fraction. Structural breakdown of the composite cathode material during charge and discharge cycling is proposed as a possible mechanism to rationalize the above results.

1. Introduction

Electrification of vehicles is in high demand to reduce our dependency on fossil fuels as well as the need for a cleaner environment. Electric vehicles need batteries that have high energy density and power density and can sustain the different charge–discharge rates, and operating conditions over different cycling periods. Lithium Iron Phosphate ($LiFePO_4$) has shown better energy density (~105 Wh/kg) and power density (>300 W/kg) than the other competing cathode materials used in Li-ion batteries designed for automotive application. $LiFePO_4$ batteries are also inexpensive, nontoxic and environmentally benign [1]. However, the aging of these batteries under typical operation cycles has been a point of concern [2]. Extensive multi-scale characterization of morphological changes in the battery cathodes has been carried out over the years, using techniques ranging from Flash Method for thermal imaging (m), Scanning Electron Microscopy (mm–μm), Atomic Force Microscopy (μm), and Transmission Electron Microscopy (nm) [3–7], with a view to provide an improved understanding of aging mechanisms in these systems. Multi-scale characterization would help link evolution at the microstructure to system level performance metrics such as capacity and power fade and hence provide insights into battery aging and improved battery design. The multi-scale morphological studies have shown coarsening of nanoparticles during the aging of the batteries [3–7]. Nagpure et al. [3] have provided evidence for the coarsening of $LiFePO_4$

* Corresponding author.
E-mail address: nagpure.1@osu.edu (S.C. Nagpure).

0378-7753/$ – see front matter © 2013 Elsevier B.V. All rights reserved.
http://dx.doi.org/10.1016/j.jpowsour.2013.06.023

nanoparticles in the cathode through scanning electron microscopy (SEM) imaging, as shown in Fig. 1. In their paper, they demonstrated a six-fold increase in particle size distribution with aging and used this observation to explain the results from thermal diffusivity experiments. A change in particle size would result in a change in porosity. Nagpure et al. [3–7] based on these findings have proposed change in porosity of the composite cathode material during aging. The key factor influencing battery performance is the Lithium intercalation/de-intercalation capability of the electrodes [1]. The cathode is composed of nanoparticles of $LiFePO_4$ with a carbon coating [8]. The change is porosity leads to change in the interface carbon coated nanoparticles and the electrolyte percolating through the pores of the composite cathode affecting Lithium intercalation efficiency during cycling. Hence, characterizing and quantifying porosity (i.e. 1 − packing factor) becomes important in understanding battery aging.

X-Ray tomography has been previously utilized to characterize battery graphite anodes of Lithium cobalt oxide batteries harvested from a Lishen 18650 cylindrical cell [9], to study pore size distribution, pore interconnectivity and tortuosity. The study found a bulk porosity of 15.4%, with 95% of pores percolating through the sample. In this paper, we use non-destructive X-Ray micro-CT technique to determine the packing factor/porosity of several cathodes harvested from batteries aged under varying conditions. Subsequently, we performed X-ray diffraction (XRD) on the same samples, to observe the $LiFePO_4/FePO_4$ phase fraction as a function of aging, in order to relate the observed changes in packing factor of the cathode as a function of aging and location on it, to the phase composition. XRD has been used to study $LiFePO_4$ battery cathodes for several reasons, including the composition verification of freshly synthesized $LiFePO_4$ [10–12], to the demonstration of the role of fundamental phenomena, such as misfit strain, in battery cycling [13] and the validation of entire models proposed to explain cathode functioning [14].

2. Experimental procedure

The tomography samples were harvested from commercial cylindrical cells (26,650 size) with nominal capacity of 2.3 Ah and nominal voltage of 3 V. In these commercial cells the graphite negative electrode is bonded onto a copper substrate, and the positive electrode is formed by a porous layer of $LiFePO_4$ nanoparticles (40–50 nm) bonded onto an aluminum substrate using a polyvinylidene difluoride (PVDF) binder. The electrolyte used in this cell is a lithium hexafluorophosphate ($LiPF_6$) salt in 1:1 ethylene carbonate and dimethyl carbonate.

Four aging conditions were chosen based on varying C-rate (Table 1). The cycling of the cells was terminated when the cells reached ∼80% of their rated capacity. This protocol was found to be consistent with the automotive industry standard, which considers a cell to be dead when its capacity drops below 80% of the original rating [20].

The cells were completely discharged after they reached the ∼80% of their rated capacity. The cylindrical cells were then opened in a glove box filled with Argon atmosphere. The oxygen level was maintained at ∼88 ppm and the dew point was ∼ −34 °C. The cell was unrolled, and the long anode and cathode strips were separated. The cylindrical shaped cell shown in Fig. 2a is unwrapped into a rectangular sheet (Fig. 2b). Five regions of interest were marked on this sheet. Location 1 is closer to the periphery while location 5 is closer to the center. Samples are harvested from location 1 and 5 for each battery. Circular samples of 1.5 mm in diameter were harvested as shown in Fig. 2c, from the unwrapped cylindrical cathode using a TEM sample preparation punch. A side view of this harvested sample in Fig. 2c shows that the sample is about 0.2 mm in thickness. The cross-section of the cathode consists of an aluminum current collector at the center, sandwiched between two $LiFePO_4$ layers held to the aluminum current collector using PVDF binder.

2.1. X-ray micro-CT

X-ray micro-CT was performed using a Bruker high-resolution micro-CT Skyscan 1172 scanner. It has an X-Ray tube with a Tungsten target as a source and an 11MP CCD detector. The instrument is capable of imaging at resolutions as low as 0.88 μm. Imaging resolution is based on object distance from the detector and is increased as the object-detector distance is reduced. The circular samples were mounted in an acrylic container between Styrofoam™ layers (used to hold the sample in place). The sample was mounted on a stage that rotates about a vertical axis (see step d in Fig. 2). The sample stage lies between the X-Ray source and a CCD detector. The X-Ray tube produces a cone beam which envelopes the sample. The sample rotates at a fixed step rate within the beam as the detector collects raw images of the sample shown in Fig. 2e. The collected raw images of the sample captured by the CCD detector are then fed into the reconstruction software

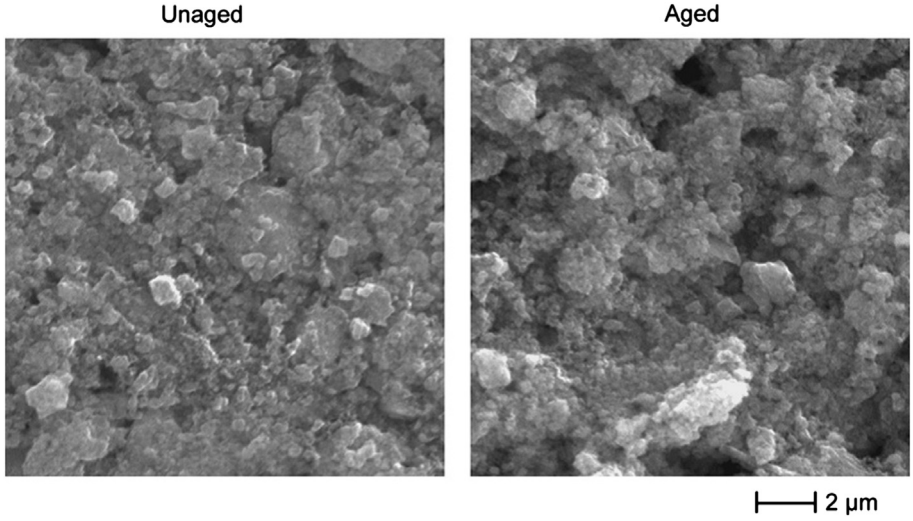

Fig. 1. SEM micrographs of unaged and aged $LiFePO_4$ battery cathode samples [3] demonstrating the previously observed coarsening effect.

Table 1
Details of the aging conditions for the batteries from which the cathode samples were harvested.

Cells	C-rate	SOC (%)	Temperature(°C)	Ah removed	Location*
C0	Unaged	–	–	0	1.5
C2	2	0–10	55	5830	1.5
C4	4	0–10	55	5540	1.5
C7	~7	68 ± 7	45	3441	1.5

* Location 1 = close to periphery of cylindrical battery, Location 5 = close to center of cylindrical battery.

NRecon®, that produces vertical sections of the 3D object shown in Fig. 2f.

2.2. X-ray diffraction

A Scintag™ RD 2000 XRD spectrometer, with a copper target source operating at the Cu K-α wavelength was used to analyze the samples. An operating voltage of 45 kV and filament current of 20 mA are used as working conditions for the experiment. 3 × 1 cm samples of the cathode were prepared from the same samples used in micro-CT experiments. They were made as flat as possible and scanned at a scan rate of 1°/min between the 2θ range of 14–70°. A two-phase Rietveld analysis was performed on all obtained spectra using the MAUD® program. Quantitative phase information was obtained for each sample along with the corresponding errors.

3. Results and discussion

For the $LiFePO_4$ cathodes, typical pore sizes are of the order of 45–250 nm, a range much smaller than the best resolution (0.88 μm) of our instrument. This makes it impossible for us to directly measure the particle size distribution and porosity of the composite $LiFePO_4$ cathode. Hence, we perform an indirect measurement, by measuring the bulk packing factor (i.e. 1 − porosity) within a voxel of size 0.88 μm^3. This is defined as indirect measurement, as packing factor values are deduced by measuring the effective attenuation value over a voxel, compared to being able to actually see the pores and calculating volume fraction. For a given sample size, the number of voxels (5×10^8) are expected to be higher and therefore the packing factor analyses is statistically significant. Despite indirect measurement, X-Ray micro-CT helps us characterize the sample over a range of length scales, from microns to millimeters. Each pixel on the reconstructed image (Fig. 2f) represents the value of linear attenuation coefficient at that x, y, z location of the object. This is based on Beer's Law, where transmitted and incident intensities are related by attenuation coefficient (μ) as:

$$I = I_0\, e^{-\mu x} \tag{1}$$

where x is the thickness of the sample, I = transmitted intensity, I_0 = incident intensity. As the sample is rotated in steps of 1°, two-dimensional projections (raw images, Fig. 2d) of it are captured by

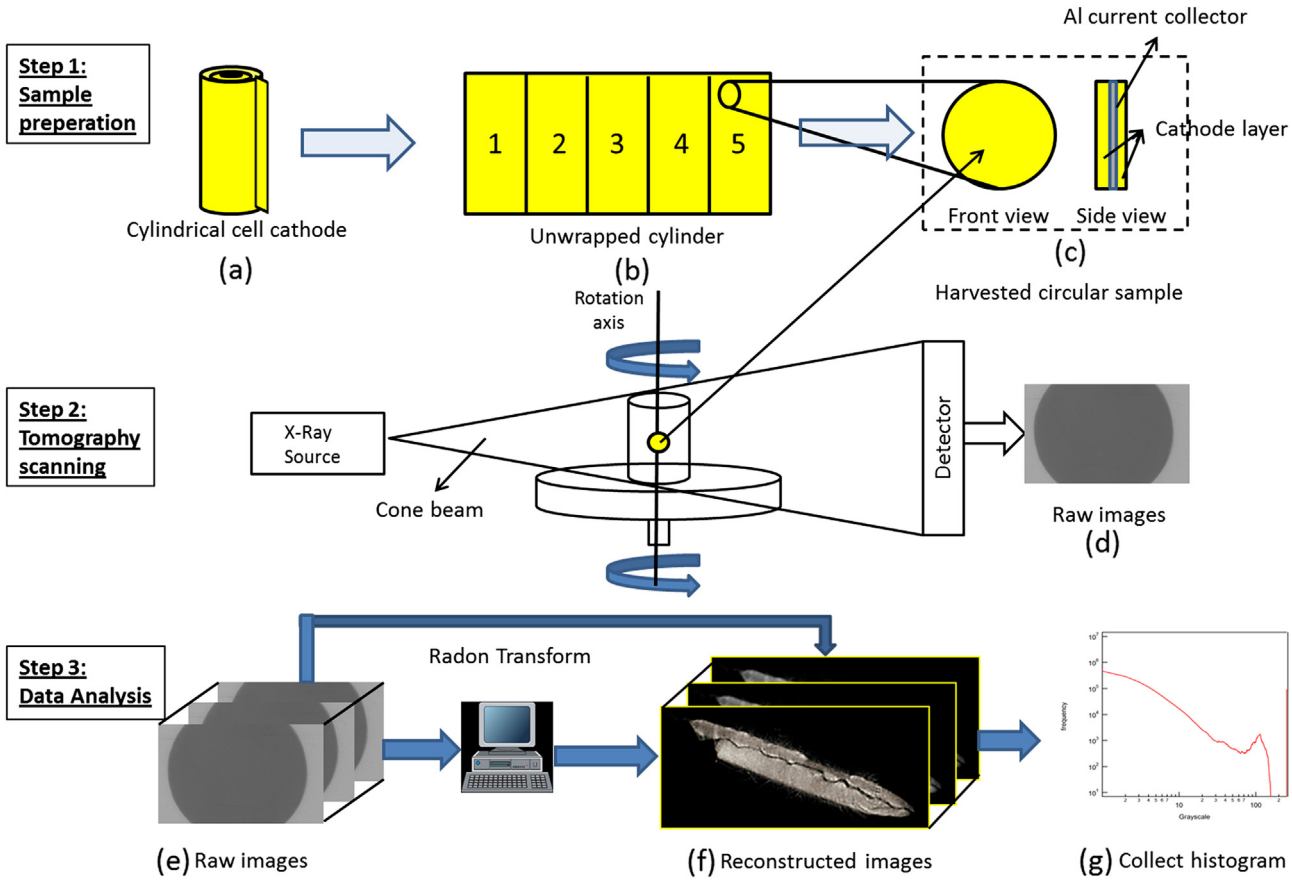

Fig. 2. Schematic representing experimental procedure flow in X-Ray micro-CT, with sample preparation, data collection and data analysis stages. (a) Cylindrical cathode from the cylindrical commercial Li-ion battery. (b) Unwrapped cathode from the battery. (C) Cross-section schematic of the cathode. (d) Schematic of the X-Ray micro-CT principle with a sample raw image. (e) Series of raw images collected in one experiment. (f) Reconstructed images of the sample using NRecon® software that reconstructs the original object by applying the Inverse Radon transform. (g) An "integrated histogram" (frequency vs. grayscale) of 1913 reconstructed images for a sample.

the detector. Projections are similar to the two dimensional X-Ray images of a patient obtained in a doctor's clinic. As the projections of the object from each rotation step are combined, enough information exists to reconstruct the original object using the Inverse Radon Transform. The reconstruction software NRecon® reconstructs the original object by applying the Inverse Radon transform on the projections (Fig. 2e) ultimately providing a series of grayscale images (Fig. 2f), which when stacked up, form the original object. Grayscale values for each pixel on these images are proportional to the linear attenuation coefficient at that point of the object being scanned. Hence, the grayscale images are maps of linear attenuation coefficient as a function of position ($\mu(x,y,z)$). In other words,

$$\mu \propto \text{grayscale value(GS)} \tag{2}$$

Possible errors that could arise due to the instrument are beam hardening and ring artifacts. Beam hardening occurs due to higher absorption of lower wavelengths by the edges of the sample. Ring artifacts arise due to defects in the CCD detector array. Beam hardening shows up at the edges of the sample by making them appear brighter while ring artifacts penetrate the reconstructed images. As such beam hardening and ring artifact correction algorithms within the reconstruction software was applied. As the pixels of a reconstructed image are represented by a grayscale value between 0 and 255, a variation in attenuation can then be related to a variation in grayscale value for the corresponding pixel. The weighted attenuation coefficient law can be used to generate a relation linking grayscale, attenuation coefficient, and packing factor. A simple analytical form of this relation is derived below. The following abbreviations have been used: μ = attenuation coefficient; w = weight fraction; Subscripts: $LiFePO_4$ = L; $FePO_4$ = F; pores = P; GS = Grayscale.

The weighted attenuation coefficient law for a multi-component material can be defined as:

$$\mu = \mu_L w_L + \mu_F w_F + \mu_P w_P \tag{3}$$

where μ_i, w_i are the attenuation coefficient and weight fraction of respective components. In our model, we use the assumption that the attenuation coefficient of $LiFePO_4$ and $FePO_4$ is the same, an assumption that is valid based on data for attenuation coefficient of these materials at the tungsten k-alpha edge (59.31 KeV), obtained from the NIST XCOM database [16]. With this assumption, $LiFePO_4$ and $FePO_4$ occupy a combined weight fraction, the rest of the weight being occupied by pores.

$$\mu(LiFePO_4) \approx \mu(FePO_4) = \mu_L \tag{4}$$

Based on this assumption, our sample effectively reduced to a two component sample, made up of a combined weight fraction of $LiFePO_4$ and $FePO_4$ (w_L), and a weight fraction of pores (w_P). Absorption due to aluminum and carbon at tungsten k-wavelengths is negligible, hence neglected into equivalent attenuation coefficient calculations. Considering the two component sample:

$$w_L = 1 - w_P \tag{5}$$

Substituting (4) and (5) in (3):

$$w_P = (\mu - \mu_L)/(\mu_P - \mu_L) \tag{6}$$

Using the previously defined proportionality between attenuation coefficient and grayscale value, Eq. (6) can be rewritten as:

$$w_P = (GS - GS_L)/(GS_P - GS_L) \tag{7}$$

Packing factor and porosity are easily interchangeable as pores are the difference of the entire sample volume and the amount of material packed into it. Each voxel (a 3D pixel) is made up of some fraction of $LiFePO_4$, $FePO_4$ and pores as shown in Fig. 3. The presence of $LiFePO_4$ and $FePO_4$ was assumed based on the two-phase theory where each nanoparticle consists of an outer $FePO_4$ shell, with an $LiFePO_4$ core, separated by a phase boundary [1]. The size of this changing phase boundary is determined by the extent of intercalation/de-intercalation of Lithium within the sample [1].

The next step in the analysis was to process the data obtained from the reconstructed images, to extract statistical information on porosity distribution within each sample. This was done by choosing a fixed volume of each sample that is considered for analysis remains constant. Prior to reconstruction, a raw image that was parallel to the detector was chosen. On this image the diameter of the sample was located, and subsequently, 767 slices above and 1146 slices below it are chosen. The raw images for a given sample are then reconstructed and only the above-mentioned slices chosen for further statistical analysis. The same number of total slices (1913) about the diameter was chosen for each sample, for analysis to make sure a fixed volume is sampled in each analysis. Then, each image in a set of reconstructed images for each sample was converted into its corresponding frequency-grayscale histogram. Histograms obtained from each slice of a given sample are added to form an "integrated histogram" (Fig. 2j). The integrated histograms are normalized to the maximum frequency in each case. Using Eq. (2), the grayscale axis of the integrated histogram was converted to packing factor. Porosity was then calculated as the difference of unity and the packing factor. Thus integrated histogram presents a statistical representation of porosity distribution of the volume sampled.

The above steps are repeated for all eight samples described in the sample set and the integrated histograms are plotted in a combined fashion, based on location on cathode and aging as shown in Fig. 4. Gaussian peak fitting is performed on each peak and statistical data such as peak position, variance, FWHM are extracted. Peak position provides the highest frequency porosity value of the sample. Variance and FWHM provide information on the distribution of porosity values within a sample. Due to the rapid decline of frequency values away from the peak value and a relatively constant variance (apart from the C7 sample in location 5), we chose to use the highest frequency values of porosity for a given sample for further analysis. The results are tabulated (Table 2) and

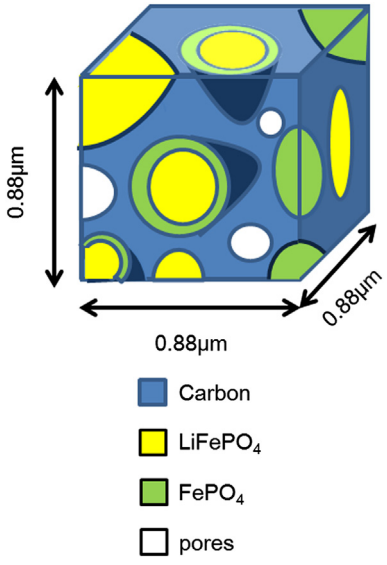

Fig. 3. Schematic of a voxel showing the co-existence of $LiFePO_4$, $FePO_4$, Carbon and pores in the composite cathode.

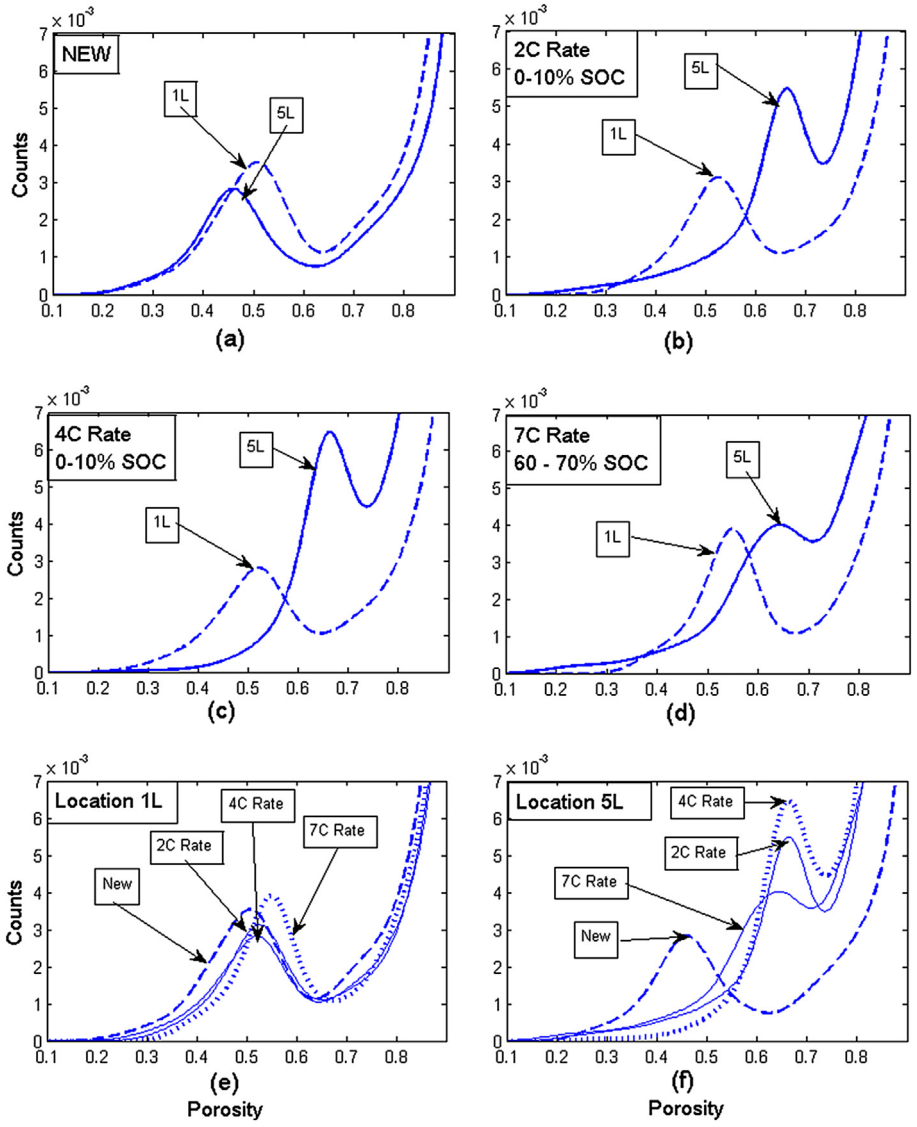

Fig. 4. Normalized integrated histograms showing variation in porosity between location 1 and location 5 within a battery sample, demonstrating an increase in porosity away from the center of the battery (except in the unaged battery case) (a) C0, (b) C2, (c) C4 and (d) C7; normalized integrated histograms showing variation at different locations for the set of batteries (e) location 1 and (f) location 5 . No change in porosity is observed at location 1 while the porosity increases at location 5 with aging at different C-rates.

further analyzed. In Fig. 4a–d, the first four plots (a, b, c and d) are normalized integrated histograms representing porosity distribution at location 1 and location 5 for a given aging condition, while plots in Fig. 4e,f are normalized integrated histograms representing porosity variation on a given location, with different aging conditions.

The results of peak fitting (Table 2) indicate a change in porosity between different cathode locations on the same battery. This can be explained by the geometry of the cylindrical battery. The jelly roll style of packing in a cylindrical battery may induce higher stresses toward the center of the battery compared to its periphery, accounting for the variation in porosity. These stresses are due to electrode stacking and dimensional changes through phase transformation during Lithium intercalation/de-intercalation within the electrodes. Peabody et al. [17] have shown that such stresses can cause accelerated aging via a pore closure mechanism within the separator. In the unaged cell the changes in porosity are too small to be conclusive. The change in porosity in the unaged condition could be correlated to inherent variations due to manufacturing practices. However, the change in porosity between the locations becomes more pronounced as the battery is cycled. Electrode stacking stress and intercaltion–deintercalation stresses might act together at these C-rates to create the noticed changes in porosity. Thermal gradients across the diameter of the cylindrical battery could also be responsible for the noticed change in porosity across locations on a cycled battery. For a given location on the cathode, an increase in porosity can be noticed with aging. This becomes a more

Table 2
Integrated histogram peak fitting for porosity calculated from X-ray micro-CT images using Eq. (7).

Battery	Location 1		Location 5	
	Porosity	FWHM	Porosity	FWHM
C0	0.5059 ± 0.002	0.2125	0.4588 ± 0.0022	0.1842
C2	0.5255 ± 0.0015	0.2039	0.6628 ± 0.0024	0.2249
C4	0.5177 ± 0.0018	0.2261	0.6588 ± 0.0018	0.2086
C7	0.5490 ± 0.0011	0.1651	0.6196 ± 0.0004	0.3172

prominent trend in location 5 (closer to the center of the cylindrical battery) than location 1 (periphery of the cylindrical battery).

Proposed aging mechanisms in spinel structured oxide cathodes of Li-ion batteries are in three major regimes: structural changes during cycling, chemical decomposition / dissolution reaction [2]. It is possible that similar mechanisms of aging operate in olivine type $LiFePO_4$ cathodes. To explain the observed results in porosity, we consider the effect of structural changes arising from mechanical stresses in the cathode during cycling. Due to lattice parameter mismatch, a coherency strain exists between the two phases [18]. The repeated stressing of the lattice due to this strain with intercalation–deintercalation, as part of a charge–discharge cycle, can cause the stresses in the cathode to increase, ultimately causing separation at the carbon–$LiFePO_4$ interface [2]. This can be explained by considering the volume change of the $LiFePO_4$ lattice with intercalation (~7%), verified by XRD measurements [15]. Misfit strains at the $LiFePO_4$–$FePO_4$ interface have also been previously measured using XRD [13]. Once this separation from the carbon matrix occurs, liquid electrolyte, which previously filled the pores in the carbon layer, may or may not occupy the voids at the carbon–$LiFEPO_4$ interface (Fig. 5).

The other possibility is that liquid electrolyte continues to occupy the newly formed larger voids, only in part (Fig. 5), without the common tri-junction contact of LiFePO4, carbon and electrolyte at certain regions. How the voids would fill up with electrolyte in the newly rearranged geometry is largely dependent on the percolation properties of the porous carbon. The separation from carbon matrix could be to different extents in different areas of the interface of the $LiFEPO_4$ / carbon layer. It has been demonstrated that the interface between these three materials (a triple contact point) is necessary for the electro-chemical reaction to occur [14], the loss of which leads to a drop in capacity and cycling capability. The loss in capacity with a loss of three phase boundary can be explained considering that we do not have an effective ionic conduction channel simultaneously with an electronic conduction channel, which would be needed for proper Lithium intercalation. The separation from carbon matrix explains the observed increase in porosity with aging. On a larger scale, it accounts for spalling of the active material previously observed in thermal diffusivity studies [3]. In consideration of the above phenomena, it would be interesting to study the nature / extent of interconnectivity of pores around the $LiFePO_4$ nanoparticles as a function of aging.

Rietveld fitting and quantitative phase analysis was performed on the XRD data from same samples that were used for tomography analysis (Fig. 6). The two-phase fitting was performed using $LiFePO_4$ and $FePO_4$ as end-members. Structural data for the two phases was obtained from Anderson et al. [15]. The results of quantitative phase analysis demonstrate an increase in $FePO_4$ phase fraction with aging at a given location on the cathode. These results have been plotted in comparison to the porosity values measured at the same locations in Fig. 7. The increase in $FePO_4$ phase with aging can be explained by considering the previously proposed separation at the carbon–$LiFePO_4$ interface with aging. This separation would result in fewer regions of the cathode where a three-phase boundary is present (active material/C/electrolyte), reducing the efficiency of Li intercalation into the solid nanoparticles. This also explains a simultaneous increase in porosity and $FePO_4$ phase fraction with aging. The trends in porosity for location 5 indicate that although there is a very significant change between an unaged and C7 cell, the porosity in the C7 sample is slightly smaller than that in cells C2 and C4. It must be noted that that the cells C2 and C4 were cycled between 0 and 10% state of charge while the cell C7 was cycled between 61 and 75% state of charge during the aging experiments. This could explain an initially upward trend in

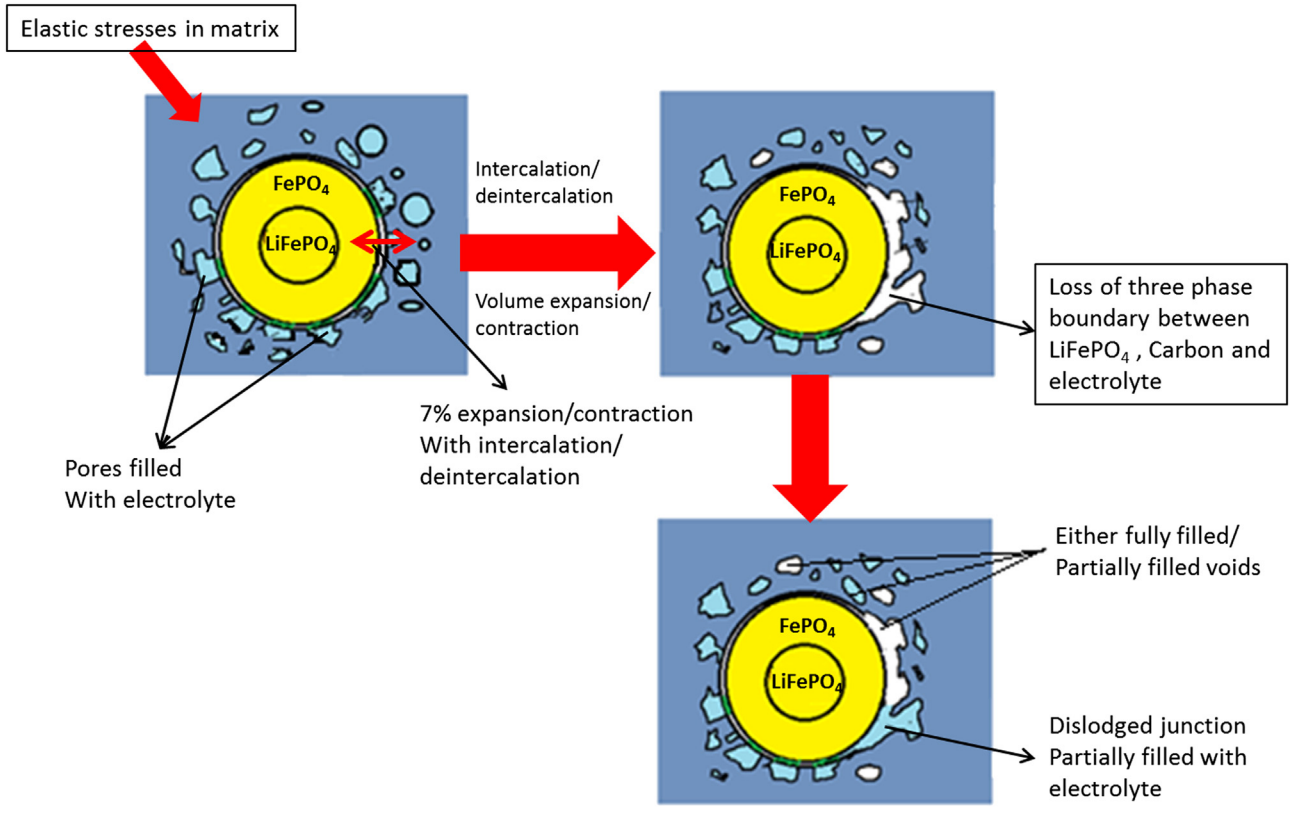

Fig. 5. Figure demonstrating carbon–$LiFePO_4$ separation hypothesis. (The size of pores has been exaggerated for demonstration of effect.)

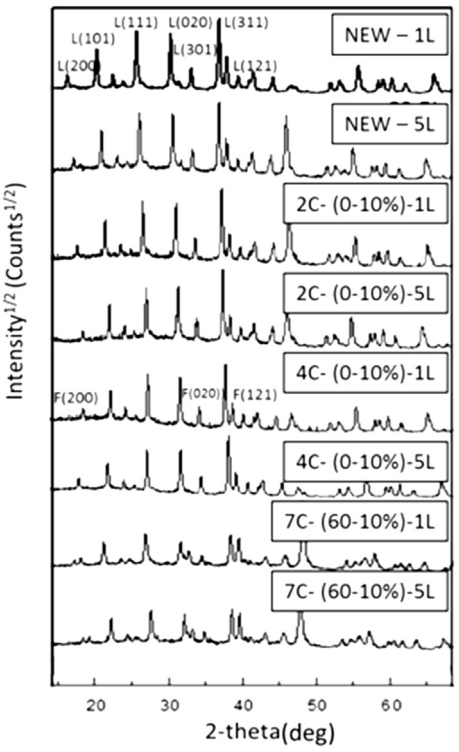

Fig. 6. XRD spectrum of the eight samples used in tomography study along with indexed reflections from different $LiFePO_4/FePO_4$ crystal planes (L = $LiFePO_4$; F = $FePO_4$).

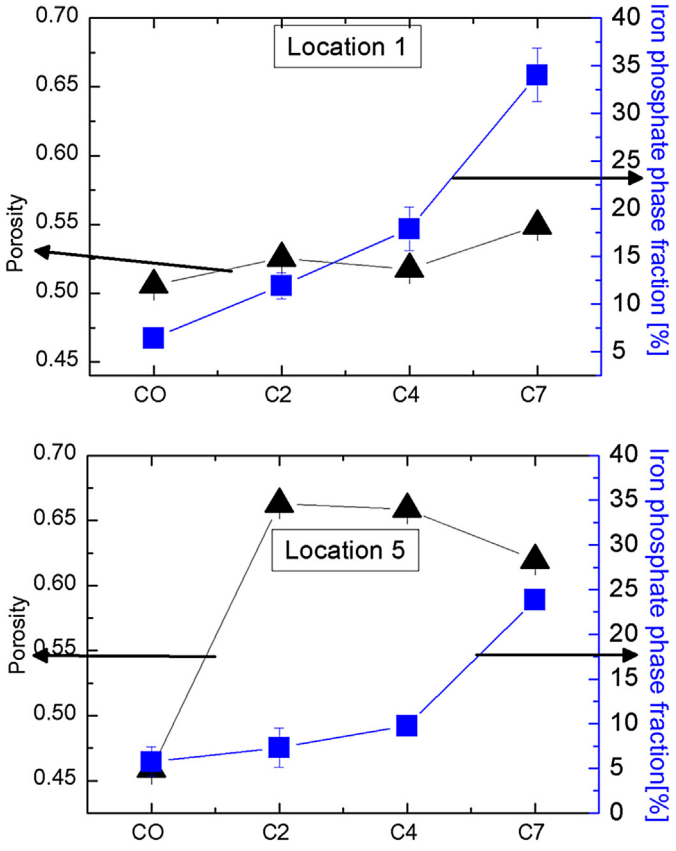

Fig. 7. Combined plots showing trends in porosity and $FePO_4$ phase fraction for locations (1) and (5) of the battery. The plots show an increase of $FePO_4$ as porosity increases with aging at a given location.

porosity that reverses slightly when moving from C-rates 2 and 4 to C-rate 7, while still maintaining a large increase (~18%) between the unaged sample and C7 aged batteries. We believe that the above data can be used to fine-tune the computational models being developed for predicting the aging characteristics of Li-ion batteries [19].

4. Conclusions

X-Ray micro-CT has been presented as a technique that can be used for the indirect measurement of the porosity of commercial $LiFePO_4$ battery cathodes without disrupting their configurations set by manufacturing practice and the emerging changes during charge and discharge cycles. An increase in porosity was measured with aging. The increase is greater in a region closer to the center of a cylindrical battery than that of the periphery. The mechanical stresses originating in the volume of the $LiFePO_4$ unit cell due to repeated cycling as a consequence of Lithium intercalation / deintercalation is suggested as a mechanism. This increase in porosity is attributed to possible separation of the Carbon - $LiFePO_4$ interface, as well as, (ionic and electronic) percolation properties of the cathode after separation of the $LiFePO_4$- carbon interface. This hypothesis is supported by quantitative XRD phase analysis showing a reduction in $LiFePO_4$ phase fraction and an increase in $FePO_4$ as a function of aging.

Acknowledgments

This material is based upon work supported by the Department of Energy, project: "U.S.-China Clean Energy Research Center for Clean Vehicles (CERC-CV)" under Award Number DE-PI0000012.

References

[1] A.K. Padhi, K.S. Nanjundaswamy, J.B. Goodenough, Phospho-olivines as positive-electrode materials for rechargeable lithium batteries, J. Electrochem. Soc. 144 (1997) 1188–1194.
[2] J. Vetter, P. Novak, M.R. Wagner, C. Veit, K.C. Moller, J.O. Besenhard, M. Winter, M. Wohlfahrt-Mehrens, C. Vogler, A. Hammouche, Ageing mechanisms in lithium-ion batteries, J. Power Sources 147 (2005) 269–281.
[3] S.C. Nagpure, R. Dinwiddie, S.S. Babu, G. Rizzoni, B. Bhushan, T. Frech, Thermal diffusivity study of aged Li-ion batteries using flash method, J. Power Sources 195 (2010) 872–876.
[4] S.C. Nagpure, B. Bhushan, S. S Babu, G. Rizzoni, Scanning spreading resistance characterization of aged Li-ion batteries using atomic force microscopy, Scripta Mater. 60 (2009) 933–936.
[5] S.C. Nagpure, B. Bhushan, S.S. Babu, Surface potential measurement of aged Li-ion batteries using Kelvin probe microscopy, J. Power Sources 196 (2011) 1508–1512.
[6] S.C. Nagpure, R.G. Downing, B. Bhushan, S.S. Babu, L. Cao, Neutron depth profiling technique for studying aging in Li-ion batteries, Electrochim. Acta 56 (2011) 4735–4743.
[7] S.C. Nagpure, S.S. Babu, B. Bhushan, A. Kumar, R. Mishra, W. Windl, L. Kovarik, M. Mills, Local electronic structure of LiFePO4 nanoparticles in aged Li-ion batteries, Acta Mater. 59 (2011) 6917–6926.
[8] Ravet, N. et al. Electrode material having improved surface conductivity. CA Patent No. EP1049182 (2000-05-02 2002).
[9] P. Shearing, L.E. Howard, P.S. Jørgensen, N.P. Brandon, S.J. Harris, Characterization of the 3-Dimensional microstructure of a graphite negative electrode from a Li-ion battery, Electrochem. Commun. 12 (2010) 374–377.
[10] M.A.E. Sanchez, G.E.S. Brito, M.C.A. Fantini, G.F. Goya, J.R. Matos, Synthesis and characterization of $LiFePO_4$ prepared by sol–gel technique, Solid State Ionics 177 (2006) 497–500.
[11] J. Gao, J. Li, X. He, C. Jiang, C. Wan, Synthesis and electrochemical characteristics of $LiFePO_4$/C cathode materials from different precursors, Int. J. Electrochem. Sci. 6 (2011) 2818–2825.
[12] Z. Chen, Y. Ren, Y. Qin, H. Wu, S. Ma, J. Ren, X. He, Y.-K. Sun, K. Amine, Solid state synthesis of $LiFePO_4$ studied by in situ high energy X-ray diffraction, J. Mater. Chem. 21 (2011) 5604–5609.
[13] N. Meethong, H.S. Huang, S.A. Speakman, W.C. Cater, Y.M. Chiang, Strain accommodation during phase transformations in olivine-based cathodes as a materials selection criterion for high-power rechargeable batteries, Adv. Func. Mater. 17 (7) (2007) 1115–1123.

[14] C. Delmas, M. Maccario, L. Croguennec, F. Le Cras, F. Weill, Lithium deintercalation in LiFePO4 nanoparticles via a domino-cascade model, Nat. Mater. 7 (2008) 665–671.
[15] A.S. Andersson, B. Kalska, L. Häggström, J.O. Thomas, Lithium extraction/insertion in $LiFePO_4$: an X-ray diffraction and Mössbauer spectroscopy study, Solid State Ionics 130 (1–2) (2000) 41–52.
[16] M.J. Berger, J.H. Hubbell, S.M. Seltzer, J. Chang, J.S. Coursey, R. Sukumar, D.S. Zucker, K. Olsen, Available [Online], XCOM: Photon Cross Section Database (version 1.5), National Institute of Standards and Technology, Gaithersburg, MD, 2010, http://physics.nist.gov/xcom [Monday, 30-Jul-2012 12:32:53 EDT].
[17] C. Peabody, C.B. Arnold, "The role of mechanically induced separator creep in lithium-ion battery capacity fade", J. Power Sources 196 (2011) 8147–8153.
[18] D.A. Cogswell, M. Bazant, Coherency strain and the kinetics of phase separation in Li_XFEPO_4 nanoparticles, ACS Nano 6 (2012) 2215–2225.
[19] J.M. Marcicki, Modeling Parameterization, and Diagnostics for Lithium-Ion Batteries with Automotive Applications. PhD Thesis, The Ohio State University, 2012.
[20] Anonymous, USABC Requirements of End of Life Energy Storage Systems for PHEVs, USABC, Southfield, MI, 2006. Available from: http://www.uscar.org/guest/view_team.php?teams_id=12.